THE THOMSON SURFACE. II. POLARIZATION

C. E. DeForest[1], T. A. Howard[1], and S. J. Tappin[2]

[1] Southwest Research institute, 1050 Walnut Street Suite 300, Boulder, CO 80302, USA; deforest@boulder.swri.edu
[2] National Solar Observatory, Sunspot, NM 88349, USA

ABSTRACT

The solar corona and heliosphere are visible via sunlight that is Thomson-scattered off free electrons, yielding a radiance against the celestial sphere. In this second part of a three-article series, we discuss linear polarization of this scattered light parallel and perpendicular to the plane of scatter in the context of heliospheric imaging far from the Sun. The difference between these two radiances (pB) varies quite differently with scattering angle, compared to the sum that would be detected in unpolarized light (B). The difference between these two quantities has long been used in a coronagraphic context for background subtraction and to extract some three-dimensional information about the corona; we explore how these effects differ in the wider-field heliospheric imaging case where small-angle approximations do not apply. We develop an appropriately simplified theory of polarized Thomson scattering in the heliosphere, discuss signal-to-noise considerations, invert the scattering equations analytically to solve the three-dimensional object location problem for small objects, discuss exploiting polarization for background subtraction, and generate simple forward models of several classes of heliospheric feature. We conclude that pB measurements of heliospheric material are much more localized to the Thomson surface than are B measurements, that the ratio pB/B can be used to track solar wind features in three dimensions for scientific and space weather applications better in the heliosphere than corona, and that, as an independent measurement of background signal, pB measurements may be used to reduce the effect of background radiances including the stably polarized zodiacal light.

Key words: interplanetary medium – methods: analytical – methods: data analysis – solar wind – solar–terrestrial relations – Sun: coronal mass ejections (CMEs)

Online-only material: color figures

1. INTRODUCTION

Coronagraphs and heliospheric imagers observe sunlight that has been Thomson-scattered off free electrons in the corona and solar wind. This effect has been used since the invention of the coronagraph (Lyot 1939), and solar wind transients such as coronal mass ejections (CMEs) have been observed with ground-based coronagraphs since the 1950s (e.g., DeMastus et al. 1973). These were accompanied by spacecraft coronagraphs in the 1970s (e.g., Koomen et al. 1975; MacQueen et al. 1974) and the coronagraph legacy continues to this day.

The physics by which this light is scattered are well established, with the original theory predating the discovery of the electron (Schuster 1879). Other important developments include the work of Minnaert (1930) and Billings (1966). The latter is the publication most commonly referred to when discussing Thomson-scattering theory with regard to white light observations. The utility of this theory to identify physical properties (such as mass) in solar wind transient phenomena (such as CMEs) observed by coronagraphs is well known. Early works include Gosling et al. (1975), Hildner et al. (1975), Rust (1979), and Webb et al. (1980). In the last decade, coronagraphs have been accompanied by another type of white light instrument. Heliospheric imagers, first SMEI (Eyles et al. 2003) and then the *STEREO*/HIs (Eyles et al. 2009), observe Thomson-scattered light at much larger angles ($>20°$) from the Sun, and their ability to track transients such as CMEs has been demonstrated (e.g., Tappin et al. 2004; Howard et al. 2006; Webb et al. 2006; Harrison et al. 2008; Davis et al. 2009; Lugaz et al. 2010). All current heliospheric imagers observe unpolarized Thomson-scattered sunlight, in part because only recently (DeForest et al. 2011) has it become clear that the bright stellar background

could be subtracted with sufficient precision for quantitative analysis of the faint Thomson-scattered signal from an imaging instrument.

Although heliospheric imagers use the same scattering physics as coronagraphs, the wide viewing angle leads to significantly different geometry and requires different treatment. For example, Thomson scattering becomes much simpler in the heliospheric case because the Sun can be treated as a near-point source, eliminating the need to carry van de Hulst coefficients (Minnaert 1930; van de Hulst 1950) when performing scattering/radiance calculations. More immediately, coronagraphs are often assumed to operate near the sky plane, but the relevant figure for a wide-field imager is the "Thomson surface" (TS) defined by the locus of the point of the closest approach to the Sun of each line of sight from the observer. That locus is the sphere with diameter passing between the Sun and the observer (Vourlidas & Howard 2006). Paper I of this series (Howard & DeForest 2012) covers the applied theory of Thomson scattering to describe the relationship between this broad-field geometry, illumination, and scattering efficiency in unpolarized heliospheric imaging, and demonstrates that a fortuitous cancellation yields a broad plateau (the "Thomson plateau") of nearly uniform-radiance sensitivity to electron density.

In the present paper, II of a series of three, we explore the consequences of Thomson-scattering theory for polarized light in the heliospheric context, and discuss scientific applications of the theory. In particular, we invert the scattering equations analytically to show how polarized Thomson-scattering imagery can be used to determine the three-dimensional (3D) location of individual small heliospheric features, without the front/back ambiguity present in similar efforts with coronagraphs (e.g.,

Dere et al. 2005), and explore analytically the limits of the technique. Further, we demonstrate via a simple forward model that the polarization signal remains present even for large features whose position cannot be found analytically. We also discuss the stability of the polarization signal from the zodiacal light and its implications for measuring the absolute radiance, rather than merely feature-excess radiance, of Thomson-scattered light from heliospheric electrons.

Polarization measurement of Thomson-scattered light observation has existed since the dawn of the coronagraph (Lyot 1933) and has been used for 3D analysis of CMEs since shortly after their discovery (e.g., Poland & Munro 1976; Wagner 1982; Crifo et al. 1983). The *Skylab* coronagraph, *Solwind*, C/P on board *Solar Maximum Mission,* and the Large Angle and Spectrometric COronagraph (LASCO) on board the *Solar and Heliospheric Observatory* (*SOHO*) all had polarizing capabilities. Perhaps because polarized coronagraph imagery, requiring photometry, is harder to work with than is unpolarized imagery (e.g., MacQueen 1993), it has not been fully exploited in the spaceflight context although recent work (Dere et al. 2005; Moran et al. 2010; de Koning & Pizzo 2011) may indicate a renaissance of polarized image exploitation in the corona.

Polarized detection of Thomson-scattered light from CMEs at wide angles from the Sun dates backs much farther than direct heliospheric imaging cameras such as SMEI and *STEREO*/HI. The *Helios* spacecraft photometers (e.g., Leinert et al. 1975) were used both to characterize the zodiacal light (e.g., Leinert et al. 1981; Leinert & Pitz 1989) and also to detect heliospheric structures via time-domain analysis of the polarized intensity signal measured by three photometers on the spinning spacecraft (Jackson 1986; Webb & Jackson 1987). Hardware on board *Helios* sorted detected photon events into accumulator bins based on their temporal phase relative to the 1 Hz spacecraft spin. These bins were accumulated to yield sky brightnesses, including polarization and color signals, on timescales of several hours. These angularly separated photometric signals were used to generate synoptic maps of the Thomson-scattering surface brightness of the solar wind (Hick et al. 1991), to estimate CME mass (Jackson & Webb 1995; Webb et al. 1995), and even to constrain coarse tomographic reconstructions of the 3D structure of the heliosphere (Jackson & Froehling 1995).

In Section 2, we discuss heliospheric imaging with polarized light in the same context as we have previously with unpolarized light (Paper I: Howard & DeForest 2012), including basic theory; importance of the TS; a summary description of instrument sensitivity, detectability, and signal-to-noise; and discussion of two key scientific applications of polarized imaging. Section 3 moves to simulations of these effects applied to non-infinitesimal features including CMEs and corotating interaction regions (CIRs). In Section 4 we discuss the applied theoretical results and their implications for future missions.

2. ELEMENTARY POLARIZED THEORY

Thomson-scattering theory has been covered at great length by many authors. Finding the polarized radiance[3] of a plasma illuminated by a distributed object that subtends significant solid angle from the scatter point (e.g., a solar coronal feature only a few solar radii above the photosphere) requires geometrical integrals over the range of solid angles of the incoming light, and is

even more complicated in the general case than is the same calculation for unpolarized light. The problem has been treated in this general case by numerous authors (e.g., van de Hulst 1950; Billings 1966; Poland & Munro 1976; DeForest 1995; Howard & Tappin 2009) as part of coronagraphic image interpretation. But in the heliospheric case the Sun may be treated as a small object, greatly simplifying the theory (Howard & Tappin 2009; Paper I). Here, we re-derive the polarized radiance formulae in this simpler case, and outline the consequences of its form for different aspects of heliospheric imaging through polarizers.

2.1. Polarized Scattering Basics

The elementary unpolarized theory of Thomson scattering begins with the differential scattering cross section for unpolarized light (Jackson 1962):

$$\frac{d\sigma}{d\omega} = \sigma_t(1 + \cos^2 \chi), \qquad (1)$$

where $d\sigma$ is the differential cross section for a single electron to scatter unpolarized light into the solid angle $d\omega$, $\sigma_t \equiv r_e^2/2$ is half the square of the classical electron radius, and χ is the angle of scatter, with $\chi = 0$ for forward scatter. Thomson scattering is absorption and re-radiation (in a dipole pattern) of incident electromagnetic radiation. The electromagnetic waves can be resolved into two polarized intensity or radiance components: $I_\perp$ or $B_\perp$ of light polarized perpendicular to the plane of scatter and $I_\parallel$ or $B_\parallel$ of light polarized in the plane of scatter. In the circularly symmetric solar case $B_\perp$ is also called the *tangential* component and $B_\parallel$ is also called the *radial* component. In local observing coordinates with the *y*-axis aligned radially outward from the Sun, the quantity $I_\parallel - I_\perp$ is the familiar "*Q*" Stokes parameter. The two components are scattered quite differently. The perpendicular component is scattered independently of χ, because of the circular symmetry of dipole radiation:

$$\frac{d\sigma_\perp}{d\omega} = 2\sigma_t. \qquad (2)$$

The factor of two reflects the fact that the perpendicular polarization is only half of the original unpolarized beam—while we are now considering a beam that is fully plane polarized perpendicular to the plane of scatter. For the parallel component, the electric field is simply projected with $\cos \chi$, so that the overall intensity is scaled by $\cos^2 \chi$:

$$\frac{d\sigma_\parallel}{d\omega} = 2\sigma_t \cos^2 \chi, \qquad (3)$$

and it should be clear that Equation (1) is simply the average of Equations (2) and (3). Coronagraphic and heliospheric imagery viewed through a radial/tangential polarizer are thus quite different from the same imagery viewed with no polarizing optics. It is most convenient to resolve observed radiance features into an unpolarized radiance $B \equiv B_\perp + B_\parallel$ and an "excess polarized radiance" $pB \equiv B_\perp - B_\parallel$ (e.g., Fisher et al. 1981). Because the propagators are linear, there is a "pB scattering cross section" made from the difference between the two polarized cross sections just as the unpolarized cross section is made from their sums:

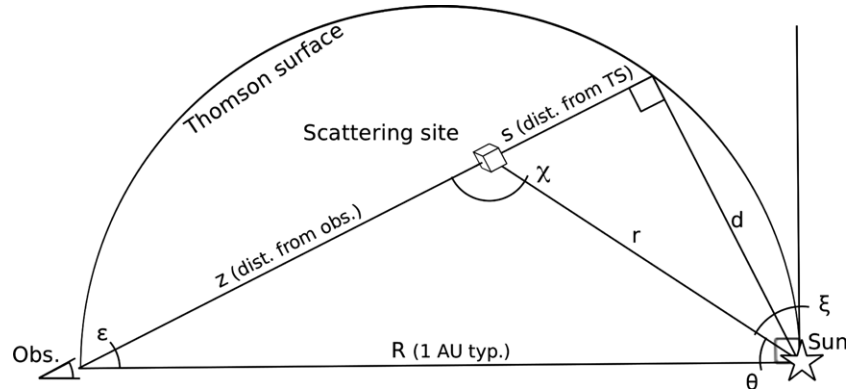$$\frac{d\sigma_P}{d\omega} = \sigma_t(1 - \cos^2 \chi) = \sigma_t(\sin^2 \chi). \qquad (4)$$

---

[3] As in Paper I, we eschew the term "brightness" that has been used confusingly in the literature to represent either radiance or intensity, even though we continue using the B and pB abbreviations (originally standing for "brightness" and "polarized brightness") for radiance.

Figure 1. Observing diagram shows relevant angles for heliospheric imaging in the context of the Thomson-scattering geometry (from our Paper I). The line of sight with elongation ε passes through the scattering site, making an angle of χ with the radial from the Sun. Distance along the line of sight is denoted s when measured from the Thomson surface and z when measured from the observer.

As in Paper I, we treat the Sun as small for the heliospheric case. This greatly simplifies the integral formulation of Howard & Tappin (2009). The scattered powers $P_\perp$ and $P_\parallel$ are proportional to the Sun's mean radiance and apparent size at the point of scatter. The excess polarized radiance is thus:

$$d\,(pB) \equiv \frac{dP_\perp - dP_\parallel}{d\omega\,dA} = \sigma_t(\sin^2\chi)\left\{\left(\frac{\pi r_\odot^2}{r^2}B_\odot\right)n_e\right\}ds,\quad (5)$$

where $r_\odot$ and $B_\odot$ are the radius and mean radiance of the Sun, ds is distance along a hypothetical line of sight, and dA is surface area normal to that line of sight. The only difference between the polarized radiance pB and the radiance B is that the $(1+\cos^2\chi)$ term from Equations (1) and (2) of Paper I becomes the $\sin^2\chi$ term in our Equations (4) and (5). Separating out the χ-dependent portion of $d(pB)$ echoes Equation (6) of Paper I:

$$d\,(pB) = k_{\mathrm{TS}}(\varepsilon)G_P(\chi)n_e(s,\varepsilon,\alpha)ds,\quad (6)$$

where ε is elongation angle, s is distance along a line of sight, α is an azimuthal angle around the Sun in the celestial sphere, and n_e is the numerical electron density across space. The in-plane geometrical values are summarized in Figure 1. The functions k_{TS} and G_P serve to isolate the χ dependence of pB. Those last two terms are given by

$$k_{\mathrm{TS}}(\varepsilon) = \left(B_\odot\sigma_t\pi r_\odot^2\right)(R\sin\varepsilon)^{-2}\quad (7)$$

and

$$G_P = \sin^4\chi,\quad (8)$$

where k_{TS} includes the χ-independent (and hence s-independent) parts of $d(pB)$, the geometric factor G_P includes the χ-dependent parts and again the geometric quantities are as summarized in Figure 1. G_P includes both illumination and scatter dependence on χ, and is sharply peaked around $\chi = 90°$. This is in contrast to the unpolarized geometric factor G, discussed in Paper I, which has an extraordinarily broad peak around $\chi = 90°$, superosculating the $f(\chi) = 1$ line there. Figure 2 shows the relationship between G and G_P. This relationship between the B and pB signals' variance with angle has been known over 60 years (van Houten 1950) and has been used to interpret coronagraph observations since at least the time of *Skylab* (e.g., Poland & Munro 1976; Dere et al. 2005). So far, it has neither been well explored nor exploited in the wide-field (heliospheric) case, which is considerably different from the coronagraph case (as described in Paper I).

The two curves G and G_P are tangent at $\chi = 90°$ because at $90°$ the Thomson-scattered light is fully polarized—so $pB = B$ at that scattering angle. The second derivative of G_P is strongly negative at the peak, so that *in pB measurements there is no Thomson plateau*, and pB measurements are most sensitive to material close to the TS. In particular, pB images are moderately well localized to the vicinity of the TS.

Considering the scattering efficiency factors in G and G_P independently of illumination, the scattering efficiency for unpolarized radiance B is minimized on the TS, while the "scattering" efficiency for excess polarized radiance pB is maximized on the TS.

The polarized excess intensity (pI) of a unit volume of material is the polarized radiance integrated over its apparent size. Carrying out the same operations as for Equation (9) of Paper I yields

$$d\,(pI) \equiv pB\,d\Omega = \left\{\frac{B_\odot\sigma_t\pi r_\odot^2}{R^4}\right\}\left[\frac{\sin^6\chi}{\sin^2(\varepsilon)\,\sin^2(\varepsilon+\chi)}\right]dN_e.\quad (9)$$

Both $d(pB)$ and $d(pI)$ for $dV = 1m^3$ and $n_e = 1\,m^{-3}$ are plotted at constant elongation ε and at constant heliocentric distance r in Figure 3, versus the out-of-sky-plane angle (or "sky angle") ξ (with the understanding from Figure 1 that $\xi = \varepsilon + \chi - \pi/2$). Figure 3 is directly comparable to Figure 5 of Paper I. The location of the TS is marked with a single vertical bar across each line-of-sight plot. The pB versus ξ curve (middle left) echoes the sharpness of the G_P geometric function in Figure 2. Unlike the unpolarized radiance B, there is no local minimum of pB at the TS in the constant-r case (upper right).

Also unlike the unpolarized case, pI has a local maximum for a given size of feature for elongation angles smaller than $30°$ (green dashed curve at lower left). At wide elongation angles, perspective effects overwhelm the Thomson scattering and illumination effects, and there is no local maximum. In all cases, perspective effects skew the location of the greatest polarized intensity away from the TS, although the greatest polarized radiance occurs on the TS. The $20°$ elongation curve, at lower left, for example, shows a peak excess polarized intensity about $10°$ closer to the observer than is the TS. At constant r, there is a local maximum in excess polarized intensity across χ at each possible exit angle. This is in striking contrast to the unpolarized case explored in Paper I, in which we showed that there is no local maximum in intensity for features with small apparent size.
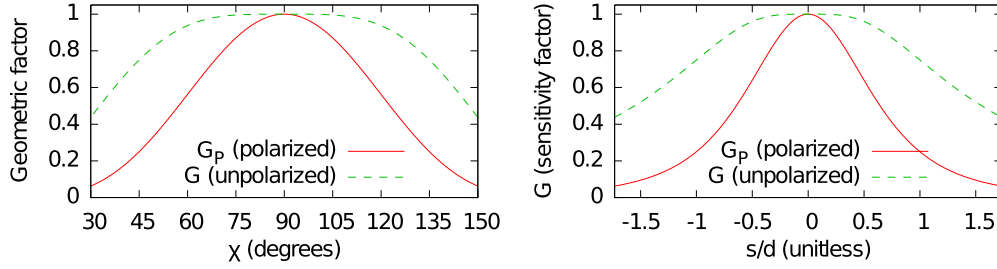
Figure 2. Comparison of the *pB* geometric factor G_P to the unpolarized *B* geometric factor *G* (derived in Paper I) in both scattering angle χ and normalized distance s/d shows sharply peaked behavior for *pB*. The sharp peak at 90° is due to the combined local maximum of illumination and the $\sin^2 \chi$ dependence of the *pB* scattering term; see Equations (4) and (5).

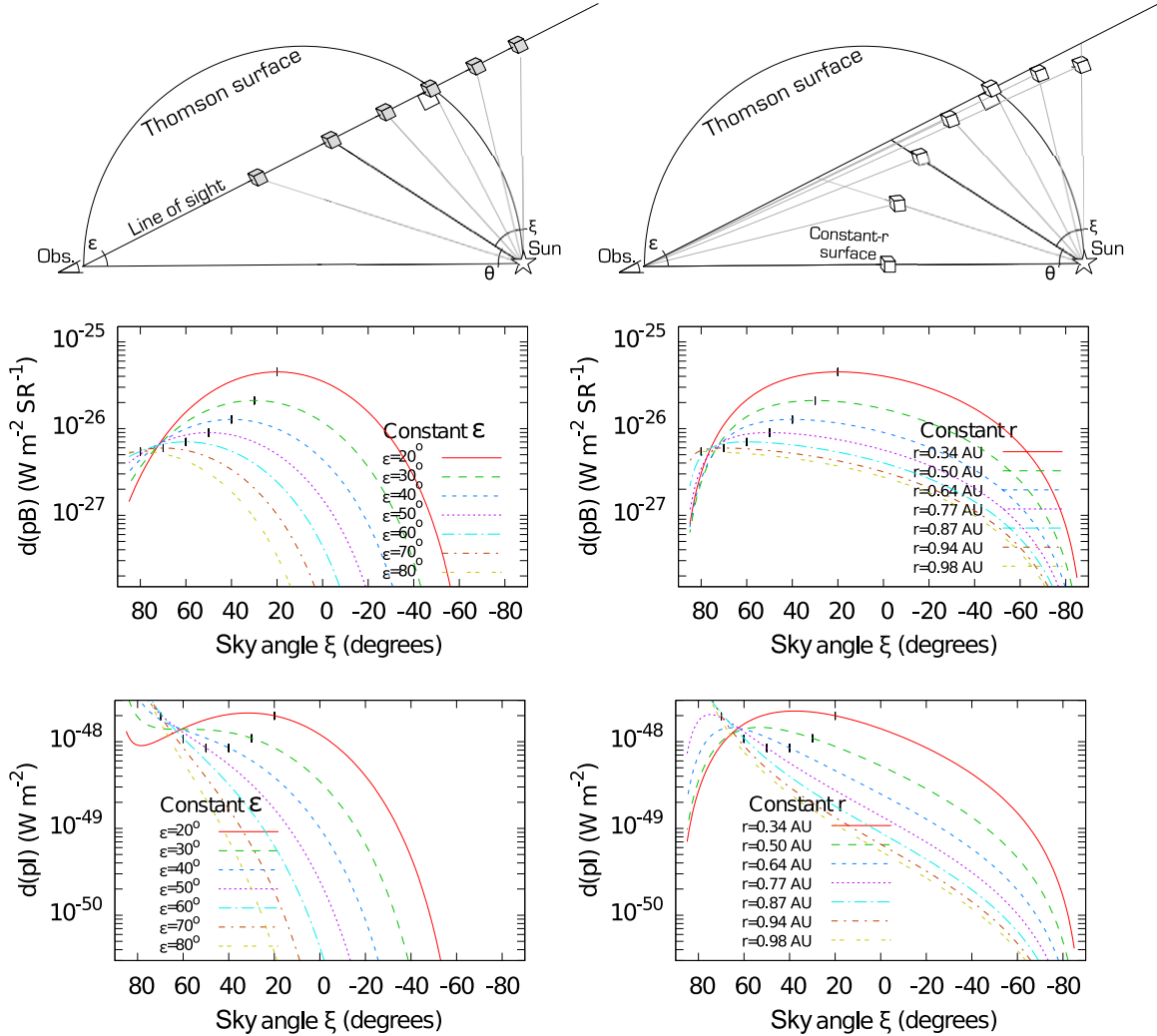(A color version of this figure is available in the online journal.)

Figure 3. Thomson-scattering effects localize the *pB* signal to the TS both at constant ε and at constant *r*. At left: excess polarized surface brightness *d(pB)* and intensity *d(pI)* at constant ε show feature contrast variation at a particular location in an instrument image plane. At right: the same quantities plotted at constant *r* show how detectability varies with exit angle. In all plots, the intersection of each line with the TS is marked. The TS marks a local maximum in *d(pB)* in both the constant-ε and the constant-*r* cases. At some (but not all) elongations there is a local maximum of *d(pI)* near (but not on) the TS (lower left).

(A color version of this figure is available in the online journal.)

2.2. Sensitivity and Signal-to-Noise Ratio

As discussed in Paper I, detectability of features visible in *pB* depends not on their radiance but on their total intensity (in this case, total polarized intensity) above a noise floor. Because *pB* and *pI* are compound measurements (they are formed from the difference between two radiances or intensities, respectively), the intrinsic photon noise for *pI* is greater than for a single measurement of $I_\perp$ or $I_\parallel$. But in the heliospheric case, intrinsic photonic noise in the intensity of the desired Thomson-scattered feature is small compared to the large background (and its associated photon and other noise sources) that must be subtracted. Even outside the brighter regions of the zodiacal light and the galaxy, the surface brightness is dominated by
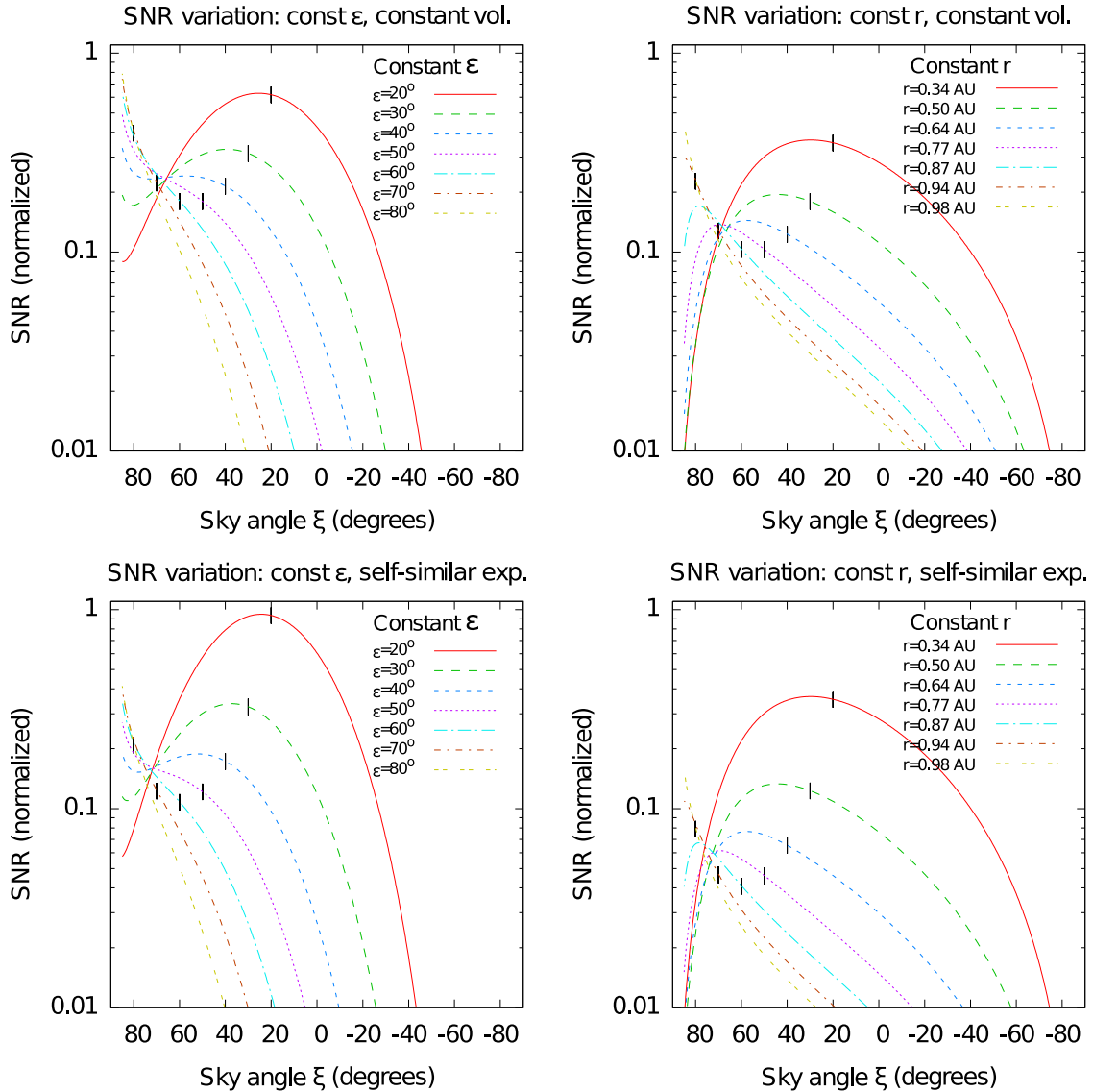
Figure 4. Signal-to-noise ratio (S/N) variation for polarized intensity vs. sky angle ξ for four cases: at left, constant-ε; at right, constant-r. At top: constant feature volume; at bottom: self-similar expansion. In all cases, the S/N drops more rapidly than in the unpolarized case described in Paper I. Observer-directed events have S/Ns reduced by a factor of order 10 compared to the ideal viewing angle. The curves have been normalized with the same coefficients as Figure 6 of Paper I, and are therefore directly comparable to their counterparts there.

(A color version of this figure is available in the online journal.)

the star field (e.g., Jackson et al. 2010). Following the analysis in Paper I, we note that the background noise against which features are measured is a random variable with approximately constant distribution, with an approximately constant number of samples per unit solid angle on the celestial sphere. This means that $N = L\Omega^{0.5}$, where N is the noise against which a feature is to be compared, Ω is the solid angle subtended by it, and L is an instrument-dependent factor. It is thus possible to calculate *a priori* how the signal-to-noise ratio (S/N) varies with geometry for any small visual feature, up to a normalization constant.

Figure 4 shows how the ratio varies for different types of feature and different types of angular comparison. The left two panels show line-of-sight comparison and the right two panels show constant-radius comparison, as in Figure 3. The top two panels show the behavior of a feature with constant volume and mass as it propagates out from the Sun, and the bottom two panels show the behavior of a self-similarly expanding feature of constant mass as it propagates outward, i.e., a feature that retains

its shape but scales to larger size with propagation as described by DeForest et al. (2012). Real solar wind features typically fall between these two cases. The self-similar expansion with constant mass is pessimistic far from the Sun as most features expand laterally but not radially as they propagate, and many dense features also accumulate mass through snowplow effects (e.g., DeForest et al. 2012). Similarly, the constant-volume expansion is somewhat optimistic far from the Sun as most features expand laterally to occupy approximately constant solid angle relative to the Sun.

Because noise analysis is strongly dependent on specifics of the instrument used to measure a signal, we confine ourselves (as in Paper I) to describing only *variation* of the S/N of a hypothetical feature across location in the heliosphere, *ceteris paribus*. Polarization measurements have additional instrument-dependent noise sources that must be considered in addition to the basics of aperture and integration time for an unpolarized measurement. In particular, an instrument that collects

individual polarized signals in sequence through a single polar-
izer will incur noise from evolution of the signal and background
between the two exposures, while instruments that rapidly mod-
ulate or that use dual-beam polarization do not, but may incur
other sources of noise. These noise sources are dependent on the
specific technology and instrument used to detect polarization,
and generally increase the denominator of the S/N, but they
do not affect the form of the variation of S/N with feature-Sun
distance.

Because of the instrument dependence of the absolute
S/N, we normalized the curves in Figure 4 to be near unity,
to display how the ratio varies for a particular class of feature.
The normalization constants for Figure 4 are numerically the
same as the normalization constants we used in the analogous
figure for unpolarized signal (Figure 6 of Paper I), and the fig-
ures may therefore be compared directly although the maximum
value in Figure 4 is not always unity. Polarized S/N is domi-
nated by the interplay of the inefficiency of the pB scattering far
from the TS, and the proximity effect in intensity as the feature
approaches the observer.

The right-hand plots show, unsurprisingly, that Earth-directed
features are not clearly visible from Earth in pB alone. Features
close to Earth are more readily detectable but that is a perspective
effect: the peaks in S/N at 60°–80° elongation in all the plots in
Figure 4 are due to large apparent-size effects in infinitesimal
features; the S/N of real features will thus roll off when the
feature-observer distance z shrinks to the same order as the size
of the feature itself: at smaller values of z, the small-apparent-
feature approximation $\Omega \propto z^{-2}$ no longer holds.

2.3. Comparison with Unpolarized Scattering: 3D Effects

Combining polarized and unpolarized imagery, with suffi-
cient S/N, enables location of features in 3D with a single polar-
ized image pair. This technique has been explored extensively in
coronagraphs in recent years (e.g., Moran & Davila 2004; Dere
et al. 2005; de Koning & Pizzo 2011). Here we develop the
theory in the slightly different case of wide-field heliospheric
imaging. The ratio pB/B (and its feature-averaged equivalent,
pI/I for a whole feature) is just the ratio of the corresponding
geometric factors:

$$\frac{pB}{B} = \frac{G_P}{G} = \frac{\sin^2 \chi}{1 + \cos^2 \chi}, \qquad (10)$$

which has solutions:

$$\chi = \mathrm{acos}\left(\pm\sqrt{\frac{1 - pB/B}{1 + pB/B}} \right) \qquad (11)$$

or, giving the sky angle ξ in terms of observed elongation angle
ε and pB/B,

$$\xi = \varepsilon + \mathrm{asin}\left(\pm\sqrt{\frac{1 - pB/B}{1 + pB/B}} \right). \qquad (12)$$

The relationship between ξ and pB/B is plotted in Figure 5 for
two different features exiting the Sun at $\xi = 20°$ (near the plane
of the sky; green in the figure) and $\xi = 80°$ (nearly directly
at the observer; purple in the figure). The two branches are on
opposite sides of the TS, equally displaced from it along the line
of sight. In the coronagraphic case, the two branches represent
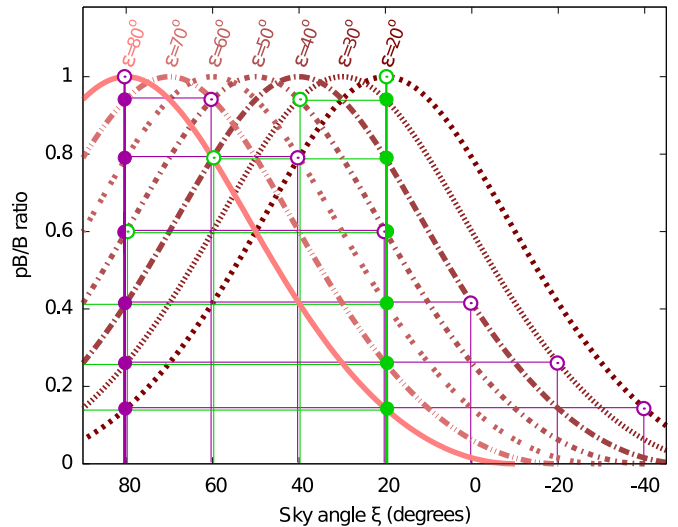a permanent ambiguity, because ε is nearly zero and therefore

Figure 5. Ratio of pB to B in small features varies with sky angle ξ, and is plotted
for several elongation angles (dashed/dotted curves). Overplotted: two example
features exit the Sun at $\xi = 20°$ (green; nearly in the plane of the sky) and
$\xi = 80°$ (purple; just missing the observer), passing through elongation angles
between 20° and 90°. At each elongation, the feature's pB/B ratio corresponds
to either the real ξ (bold vertical lines with solid circles) or to a ghost location
ξ' that varies with elongation (horizontally extended lines with open circles),
which is dynamically implausible. See Figure 6 for a sketch.

(A color version of this figure is available in the online journal.)

the TS is in the plane of the sky. In the heliospheric case, the
curvature of the TS breaks the front/back asymmetry. While any
one heliospheric measurement of pB/B cannot identify which
branch is occupied by a given feature, time series of observations
can: on the occupied branch, the trajectory is approximately
inertial and radial from the Sun, while on the opposite branch the
inferred "ghost trajectory" includes large lateral accelerations
that are reflected in the curved path in Figure 6.

Location of features in three dimensions requires propagating
noise in the photometry through the (pI/I)-to-ξ conversion
process. Neglecting instrumental noise sources, the noise level
of the (pI/I) measurement may be calculated by simple
quadrature combination of the pI and I noise sources. Treating
the noise in the first order, the feature as compact and uniform-
radiance, and the two measurements (and noise samples) as
independent, gives

$$\Delta\left(\frac{pI}{I} \right) \approx \left(\frac{\Delta pI}{pI} \oplus \frac{\Delta I}{I} \right)\left(\frac{pI}{I} \right), \qquad (13)$$

where $\oplus$ denotes addition in quadrature. The resulting noise
term can then be propagated through Equation (12) to identify
the error in ξ determination for any given noise level in the
images. The two terms added in quadrature are the S/Ns of the
pI and I measurements, respectively. This treatment glosses over
the fact that pI is a compound measurement and hence incurs two
samples of the background noise, but that makes no difference
because (1) the photon noise in the signal itself is considered
to be negligible compared to that of the background; and
(2) if pI and I are assembled from the sum and difference of two
intensities obtained through polarizers (or through one rotating
polarizer), there are still only two samples of the background
photon noise to be considered.

To understand the behavior of actual 3D interpretation, we
work from the perspective of trying to determine the position
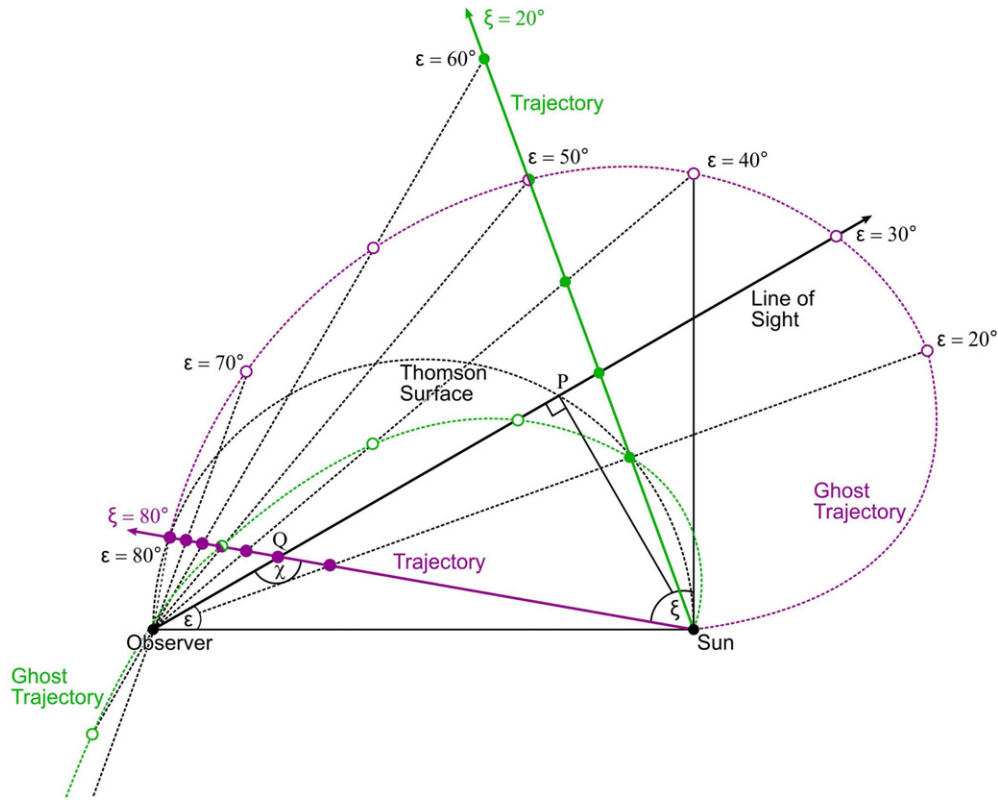of a particular feature in radial motion, whose total intensity is

Figure 6. Two feature trajectories show how feature ξ measurements relate to elongation angle ε. The green ($\xi = 20°$) and purple ($\xi = 80°$) features propagate most of 1 AU on opposite sides of the Thomson surface. The ratio pB/B (or, equivalently, pI/I) in the feature is consistent with two values of ξ at each point—but the "ghost trajectory" is unphysical. See Figure 5 for a plot of pB/B for features along each line of sight in this figure.

(A color version of this figure is available in the online journal.)

measured with a given S/N in the unpolarized channel. Figure 7 shows the calculated position of an ensemble of five small features with moderate S/N, using direct measurement of the pI/I intensity ratio.

Two of the features in Figure 7 correspond to the two features followed by Figures 5 and 6. All of the features were treated as self-similarly expanding, with an average S/N across each of the two polarized channels of 10, 30, and 100 at 0.8 AU from the Sun. The three S/Ns yield three sets of error bars on the inferred value of ξ; these error bars are represented with the nested semitransparent curves around each ξ trace. To find the S/N at each value of r, we used the same formulae as for Figure 4 (and for the I measurement using the formulae for Figure 6 of Paper I). For example, following the green trace we observe that a feature leaving the Sun at $\xi = 20°$ that happens to have an S/N of 10 at elongation $\varepsilon = 45°$ can be determined from a single pI/I measurement to have ξ either between $15°$ and $25°$ or between $67°$ and $73°$. The same feature with an S/N of 30 or 100 has similar inferred locations but tighter error bars.

The shapes of the measurement loci in Figure 7 are dominated by the two branches of the ξ calculation in Equation (12). Since the features propagate radially, the correct branch yields ξ determinations that are constant as the feature propagates outward through different elongations, while the ghost trajectory (Figure 6) yields rapidly changing ξ angles versus elongation ε as the feature propagates. The intersection of the two branches occurs at the TS, which is marked with a dashed black line. The plot thickens there, primarily because the pB/B ratio is independent of ξ at the TS. The two branches are symmetric

about the TS because of the symmetry of the G and G_P functions around $\chi = 90°$ (Figure 2).

All of the features in Figure 7 show greatly increased uncertainty toward the right of the plot, reflecting the fact that the feature grows both fainter and farther from the observer as it propagates away from the Sun. The $\xi = 0$ curve, in particular, has error bars that grow to over $\pm 45°$ around the true measurement at around $\varepsilon = 60°$, as the S/N drops below unity: in that geometry, the feature is 2 AU from the Sun and 2.2 AU from the observer.

The feature in Figure 7 with the least uncertainty is at $\xi = 80°$, headed nearly directly toward the observer. For that geometry, perspective effects oppose the illumination effects (though do not exactly cancel them) through the mid portion of the trajectory. Hence, the S/N remains high throughout the $\xi = 80°$ trajectory, and the error bars remain small except for the intrinsic uncertainty near the TS.

The error bar shape is dominated by the computed S/N of the feature: brighter, more compact features yield lower error bars, and fainter, more diffuse features yield larger ones. In particular, we have used self-similar expansion with constant N_e (total electron count) in the feature to scale the error bars as the features propagate outward; this approach may be slightly pessimistic on the right-hand side of the plot when compared to actual feature behavior, as discussed in Section 2.2.

Real polarizing instruments may be subject to additional noise sources that are more complex than the simple model we have used. Calibration errors between the two channels would introduce noise that scales with the background and
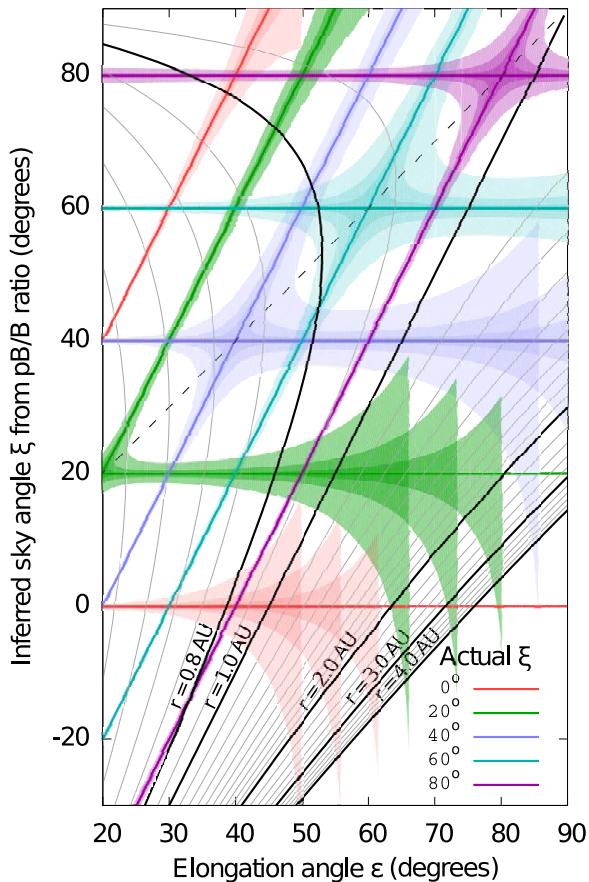
Figure 7. Inferred sky angle ξ vs. elongation ε for five small features with moderate S/N, using direct measurement of the pI/I intensity ratio. The inferred physical (horizontal) and ghost (diagonal) trajectories are solid lines colored by feature. Shapes around each line are ξ error bars for self-similarly expanding features with three S/Ns at 0.8 AU: 10 (wide), 30 (medium), and 100 (narrow). The green and purple features are also shown in Figures 5 and 6. The Thomson surface ($\xi = \varepsilon$) is marked as a dashed black line, and curves of constant radius from the Sun are marked as solid black curves.

(A color version of this figure is available in the online journal.)

behaves functionally the same as the noise calculations we have used, and therefore do not affect Figure 7. Simultaneity errors could arise in instruments that measure the two signals at slightly different times. These types of errors yield noise that is directly proportional to the signal being measured and inversely proportional to the timescale of its evolution, and therefore they would soften the curves in Figure 7, by fading with distance from the Sun even as the main noise source (background) increases with feature size.

We conclude that pB/B measurement of individual features' excess radiance over background could be used to infer absolute exit angle from the Sun with precision of a few degrees of angle, with S/N values that are achievable with current instruments in B alone (as in DeForest et al. 2011). While any one image yields ambiguous results with two branches, time series of data reveal which of the two branches is the correct one. Near the TS, such measurements are very imprecise because the slope of pB/B with respect to the sky angle ξ is near zero—but radially propagating features necessarily spend time both near and far from the TS. Those events of primary interest to space weather prediction—those with ξ close to $90°$—yield the most precise measurements of ξ, making pB/B measurements particularly interesting for this application.

This analytic result applies only to *small* features—i.e., those for which the feature's characteristic length is negligible compared to the distances to the Sun and observer, and which may therefore be treated as point sources. We discuss measurements of large-scale features briefly in Section 3 of this paper and at greater length (and more rigor) in Paper III of this series (Howard et al. 2013).

2.4. Polarization Effects and Absolute Background

In coronagraphs, pB measurements are used to reduce unwanted background light from sources outside the coronagraph. In particular, the terrestrial sky is quite bright near the Sun, and pB measurements help to reduce that contamination by subtracting two measurements with equal amounts of background light (e.g., Lyot 1933). In terrestrial coronagraphs, the technique is limited by polarization of the sky light at angles surprisingly close to the Sun (Leroy et al. 1972). In space-based coronagraphs, the main persistent background is a combination of stray light from within the instrument itself and sunlight scattered from microscopic dust grains (the F corona and zodiacal light; we use these terms interchangeably). In the near-Sun field out to $\sim 10\ R_{\odot}$ in the sky, the F corona is nearly unpolarized, so pB measurements of the corona can provide an absolutely calibrated Thomson radiance of features in the corona. Unpolarized coronagraphic measurements such as the primary synoptic data sets from *SOHO*/LASCO (Brueckner et al. 1995) and wide-field unpolarized heliospheric images such as from *STEREO*/HI (Eyles et al. 2009) cannot in principle separate the background signal from a steady component of the Thomson radiance under study, and therefore only report a "feature-excess" radiance (e.g., DeForest et al. 2012). Here we discuss the feasibility of similar absolute calibration of heliospheric Thomson-scattered radiance from a polarizing heliospheric imager.

In a space-borne heliospheric imager, the background is a combination of stray light from within the instrument itself, the unpolarized star field, and the F corona, which ranges from $10^{-14}\ B_{\odot}$ to $10^{-13}\ B_{\odot}$ at elongations of interest to inner heliospheric solar wind studies in the plane of the ecliptic. The zodiacal light dominates the sky background by photon count, and is polarized by up to 20% with a pole-to-ecliptic radiance variation of about four times at $90°$ elongation from the Sun (e.g., Dumont & Sanchez 1976; Leinert et al. 1981, 1998). In other words, there is a background pB signal of order of a few $\times 10^{-14}\ B_{\odot}$ at moderate elongations from the Sun, compared to the Thomson-scattering radiance of a few $\times 10^{-16}\ B_{\odot}$ in typical solar wind features. Thus, even pB measurements require modeling of the diffuse background, just as do direct B measurements: individual constructed measurements include a broad diffuse background that must be subtracted from the data to yield "feature-excess" radiance in individual features.

Even with the presence of persistent diffuse background, pB affords techniques for indirect or ongoing-calibration methods to improve the modeled background, which could permit detection of absolute Thomson radiance based on the improved modeling. In particular, the *Helios* probes found that the zodiacal light is extraordinarily stable across solar wind condition (Richter et al. 1982a, 1982b) and even across the whole solar cycle. Leinert & Pitz (1989) conclude that the secular variation of the zodiacal light radiance is at most of order 1% (limited by the longevity of the *Helios* photocells) with similarly stable polarization properties. This is useful because, even with as much as 1% long-term variation of unpolarized radiance in the zodiacal light, the stable polarization properties can be used to

reduce the variation by another 1–2 orders of magnitude. Hence, once well characterized with a particular instrument, a zodiacal light model may be used to produce a stable zero point for pB measurements of Thomson scattering at the few $\times 10^{-17} B_\odot$ level for the life of that instrument.

Other types of wide-field unpolarized background are present in low-Earth orbit (Jackson et al. 2010), including high altitude orbital speed ram airglow and high altitude aurora (Mizuno et al. 2005). Both effects are thought to be unpolarized as the mechanism for each is direct atomic line emission, though to our knowledge neither has been tested. The aurora, as measured by SMEI, is comparable to the zodiacal light when observed but is not universally present. The airglow is universal at lower altitudes than that of SMEI, and 3–4 orders of magnitude fainter than the zodiacal light at the 570 km altitude of the *Hubble Space Telescope* (Brown et al. 2000).

We conclude that polarization can remove and/or stabilize at least some important background effects, affording long-term remote measurement of absolute density in the solar wind once a sufficient baseline of measurements is made. While the dominant steady diffuse light source (the zodiacal light) is slightly polarized, it has been measured to be remarkably constant in both intensity and degree of polarization; and the dominant variable diffuse light sources in low-Earth orbit (aurora and ram airglow) are thought to be unpolarized and hence not to affect absolute pB measurements, but have not yet been characterized to the precision required for such measurements. Given recent successes with separation of the heliospheric Thomson signal from F corona and stellar background based entirely on image morphology (DeForest et al. 2011) and the difference in image morphology between airglow and the K corona, it is plausible that such measurements could be made even if these terms prove to be variably polarized.

In addition to these non-Thomson-scattering background signals, there is a Thomson-scattering background to any particular feature under observation, because the heliosphere and corona are optically thin. Just as in the corona, heliospheric CMEs and other individual bright features can be many times brighter than the rest of the Thomson-scattered heliospheric signal in unpolarized light (DeForest et al. 2011, 2012), and the Thomson background can be neglected for these features; but Thomson-scattered background is important to analysis of faint features, just as it is in coronagraph data.

3. FORWARD MODELING OF HELIOSPHERIC IMAGERY

In order to gain a ready appreciation of the differences between how solar wind disturbances appear in total power and polarized radiance, we present here some simple simulations of solar wind features to approximate the qualitative behavior of the polarization signal from features with large extent. The intent of these simulations is to reveal how Section 2 changes when the features are not small—i.e., when integration, rather than simple proportional scaling, is required. The B and pB signals from large structures with nontrivial geometry contain contributions from many different ξ angles along the line of sight, and therefore do not follow the simple inversion in Figure 7. We use the simplest possible simulations to reproduce the gross morphology of several typical heliospheric structures to highlight how the overall feature shape influences the polarization signal. Quantitative analysis of more realistically simulated large-scale features is presented in Paper III (Howard et al. 2013).

We used the generation codes of the Tappin–Howard model (Tappin & Howard 2009) to compute synthetic sky maps for a number of idealized disturbances. The TH model is a code that extracts 3D parameters of CMEs by fitting simple geometric models to the evolution of the CMEs as they propagate. Briefly, a model with homogeneous solar wind density is assumed and the Thomson-scattering formulae are integrated in a spherical grid. Disturbances are added by multiplying the relevant cells in the grid by an enhancement factor. These can be bent shells that simulate CMEs (Howard & Tappin 2010) or spiral structures representing CIRs. For the purposes of this study, to simplify comparison, we only consider ecliptic plane cuts through those maps.

3.1. Small Scale (Blob or Puff)

The first disturbance considered was a small arc-shaped transient with a thickness of 0.1 AU, and a cone angle of 6° (12° total extent) in latitude and longitude, and an enhancement factor of five above the ambient solar wind density. The enhancement factor is typical of large CMEs (e.g., Liu et al. 2010; Möstl et al. 2012; Lugaz et al. 2012). The radiance was computed every 0.1 AU from 0.3 to 1.2 AU. We ran the full simulation for two longitudes in heliocentric observing coordinates, with the center of the CME at $L = 90°$ (i.e., $\xi = 0°$) and $L = 30°$ ($\xi = 60°$). The locations of the CME are shown in Figure 8 (panels (a) and (e)). Each colored sector corresponds to a location at which we computed the radiances. In panels (b) and (f) we show the excess radiance (i.e., the radiance with the quiet-wind values subtracted) for both total power and polarized radiance. In panels (c) and (g) we show the ratio of the polarized to total radiance excess, and in panels (d) and (h) the ratio of polarized to total radiance. In all of the plots, the colors of the traces match those in the schematic in panels (a) and (e). At elongations where the line of sight intersects the TS inside the transient, an overbar is placed on the plots.

This small transient can be considered to approximate a blob of plasma, and thus provides us with a clear view of the differences between observing in total power and observing in polarized radiance.

The most obvious characteristic of the excess radiance plots is the fall-off of radiance as the transient moves further from the Sun. Although the derivative of signal with respect to elongation ε is much steeper at $\xi = 0°$ (left column) than at $\xi = 60°$ (right column), that difference is primarily geometrical. Comparing the two sky-angle cases at similar radii rather than similar elongations yields a far smaller difference between the two cases, as might be expected from Figure 3.

Turning to the polarization fraction of the radiance excesses (panels (c) and (g) of Figure 8), the pB signal falls off rapidly with elongation ε for the limb transient ($\xi = 0°$) at left. But for the near-observer transient ($\xi = 60°$) at right, polarization increases to a maximum near $\varepsilon = 60°$. Both effects may be expected from Figure 3. For both transient longitudes considered here, the signal from the transient at its closest to the TS has a degree of polarization about four times greater than at its furthest.

As might be expected from the differential analysis in Section 2.1, when the transient is far from the TS and its polarization is thus less than that of the quiet solar wind, the polarization of the total received light is reduced. When it is close to the TS the polarization is increased, reaching 80% for the transient directed 60° from the plane of the sky as that transient crosses the TS.
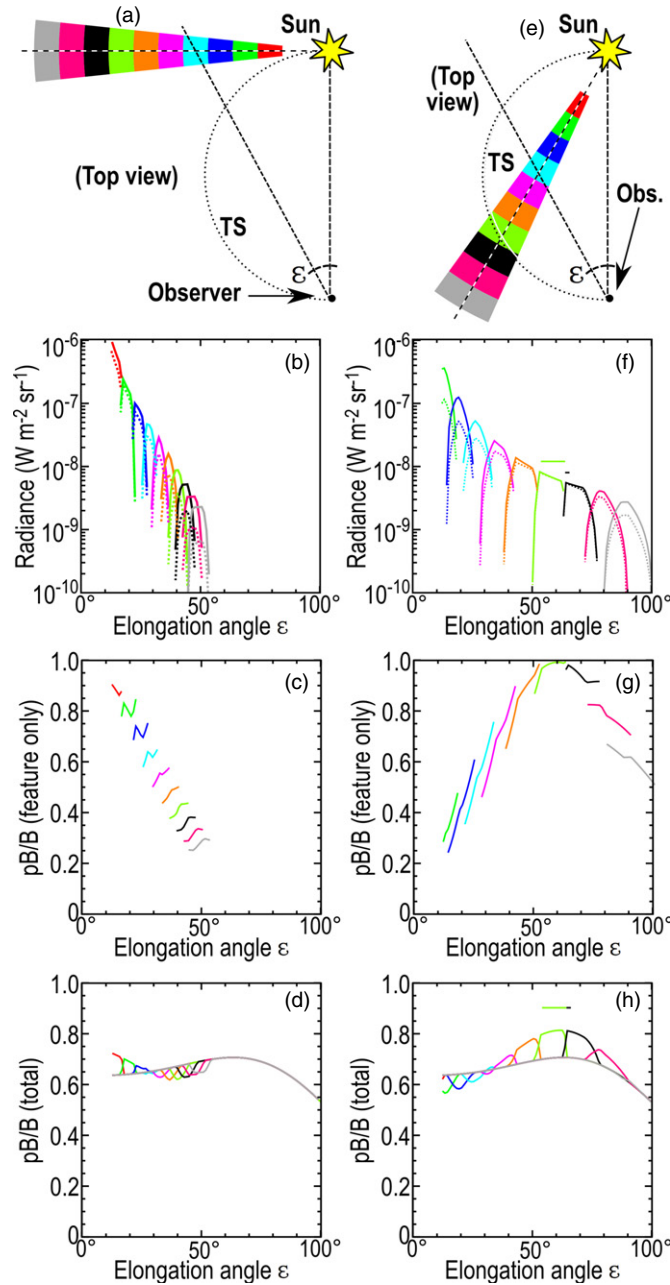
Figure 8. Radiance profiles through a small simulated transient. The left-hand column (panels (a)–(d)) shows the case of the transient in the plane of the sky ($\xi = 0°$), while the right column (panels (e)–(h)) shows the case where $\xi = 60°$. The top row ((a) and (e)) shows the locations at which the transient radiance was computed: each color corresponds to a different radius; the dashed lines show the central axis of the transient and the Sun–Observer line. The second row ((b) and (f)) shows the radiance excess as a function of elongation for each radius: the total power is solid; polarized power is dashed; the overbars indicate the elongation ranges within which the line of sight cuts the Thomson surface inside the transient. The third row ((c) and (g)) shows the ratio of feature-excess pB to feature-excess B as a function of elongation. The fourth and final row ((d) and (h)) shows the ratios of total pB to B at the feature location (without background subtraction).

(A color version of this figure is available in the online journal.)

3.2. Large Scale (CME)

We repeated the simulations of Figure 8 for a simplified conical CME with a longitudinal cone angle of $30°$, and otherwise identical parameters. The results from this cone are shown in Figure 9, in the same format as was used for Figure 8.
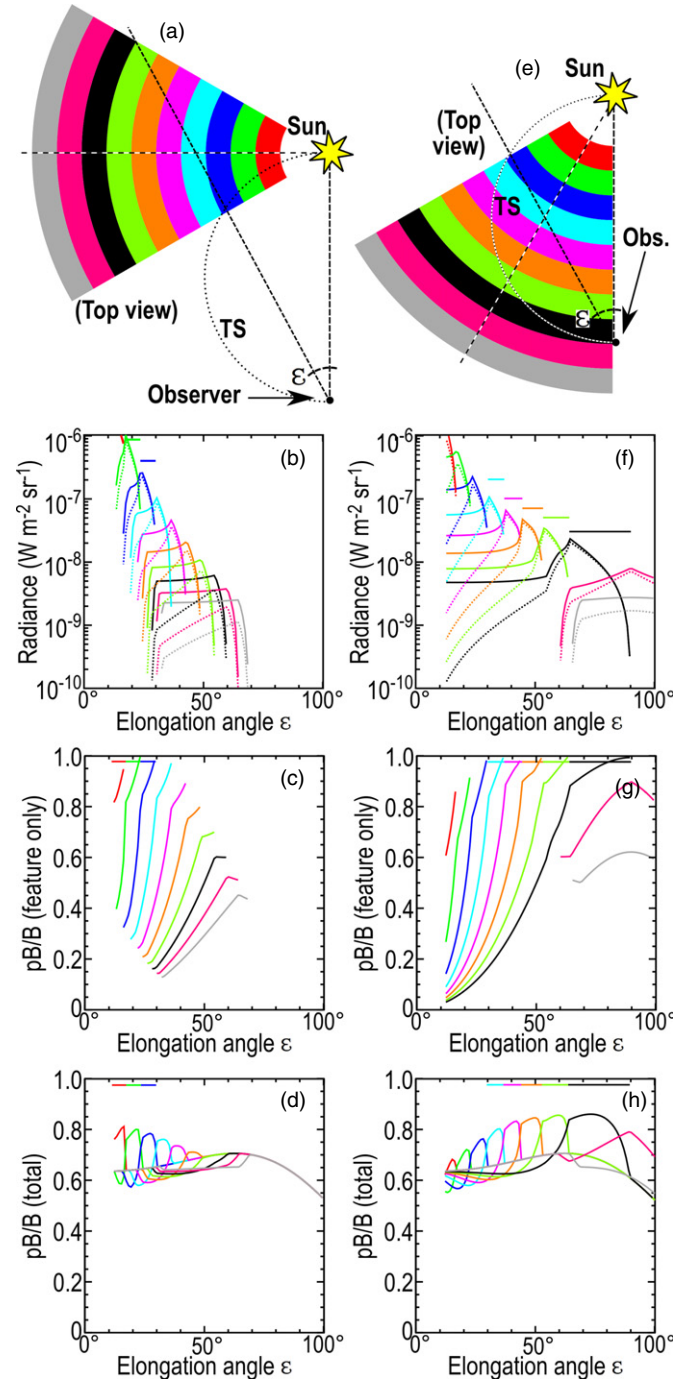

Figure 9. Display of the radiances from the large CME simulation. The format is identical to Figure 8.

(A color version of this figure is available in the online journal.)

As expected the CME appears much broader in elongation. The degree of polarization shows generally similar trends, reaching a maximum near the TS. Where the CME first intersects the TS, the highest degree of polarization (approaching 100%) occurs at the leading edge of the CME, thus producing a kind of intrinsic edge enhancement. The trailing edge, which is remote from the TS, is de-emphasized, in some cases by well over an order of magnitude. The CME directed at $30°$ always extends to the smallest elongations computed ($12°$) when it lies between the Sun and the observer. This is because this CME has a grazing impact with the observer. The extension appears as the flat tails

in the unpolarized radiance (solid) traces in Figure 9(f). In the polarized (dashed) traces, on the other hand, the radiance falls off rapidly as the scattering approaches pure forward scatter, which is unpolarized.

We conclude that the polarization signal from typical CMEs is not completely spoiled by dilution due to the large angular extent of the CMEs or the existence of a background solar wind. Further analysis is required (and is presented in our Paper III of this series) to determine how to extract CME position in three dimensions from the polarization signal.

3.3. Corotating Interaction Region

The third disturbance we simulated to generate intuition about the effects of geometry on pB was a spiral structure corresponding to a 400 km s^{-1} CIR in the plane of the ecliptic. We treated the CIR as a dense spiral structure with an extent in longitude of 24°, and increased linearly in density to an enhancement factor of three at 1.2 AU, beyond which it was of constant density. The results are summarized in Figure 10 in a similar format to Figure 8; however, here we show all elongations from −180° to +180° (with negative "elongations" corresponding to angle west of the Sun in the ecliptic, and positive "elongations" corresponding to angle east of the Sun in the ecliptic). The computations were carried out at longitudes of the leading edge of the base of 303°, 3°, 63°, 123°, 183°, and 243° relative to the observer (the 3° offset is a computational convenience). These correspond to approximately −8.5, −4, +0.5, +5, +9.5, and +14 (−13) days from the arrival of the CIR at the observer.

Again, at elongations where the line of sight intersects the TS inside the CIR or close to it, the polarization is high (approaching 100%), while at elongations where the line of sight intersects the TS far from the CIR the polarization is far less pronounced even if the unpolarized signal is strong.

A major difference in polarization behavior between the CIR and the earlier two cases is that when the CIR is growing in the eastern part of the image (i.e., approaching in the east), the polarization at the leading edge is persistently low (Figures 10(c) and (d)), while the CME and compact structure display a maximum in polarization if and when they pass through the TS. This is a direct result of the geometry of a CIR: the tangential contact between the line of sight and the CIR is dependent on the spiral angle of the CIR, and is always far from the TS, whereas for most CMEs, when inside 1 AU, the tangent point is generally close to the TS. See Figure 10 of Paper I for plots showing the distance of the CIR leading edge from the TS.

We conclude that although CIRs should be visible in polarized as well as unpolarized light, they behave differently from other types of feature because of their stationary, spiral shape. In particular, the polarization behavior of the front of a CIR is quite different from that of a localized structure such as a CME. CIRs should thus prove directly recognizable by inspection of polarized images, even without detailed inversion for 3D structure.

4. DISCUSSION

We have developed an appropriately simplified theory of polarized Thomson-scattered imaging in the heliosphere and shown that sensitivity of pB measurements to electron density is well localized along the line of sight at the TS, in contrast to the Thomson plateau observed via unpolarized light (B). For unpolarized detection, the illumination function and scattering
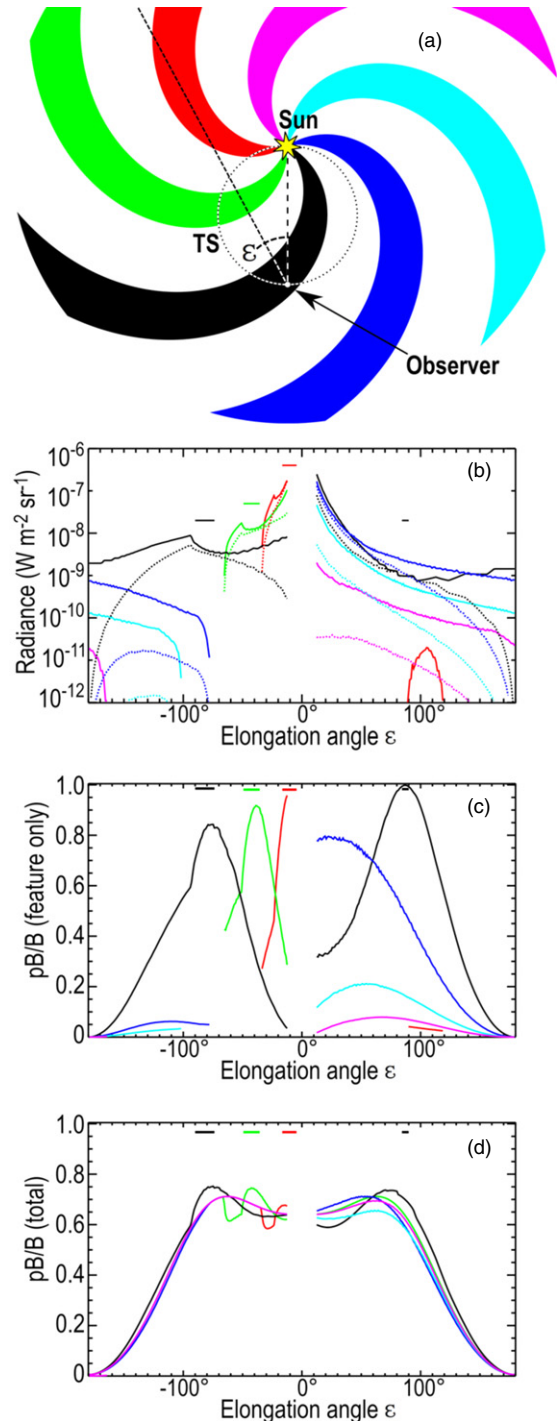

Figure 10. Display of the radiances from a simulated CIR. The format is similar to that of Figure 8, with the colored spirals representing the locations of the CIR at which the simulations were performed. Since the CIR moves from east (left) to west (right) and is not symmetrical, we show both sides of the Sun in the plots. Also the computations are continued all the way to 180° elongation. The elongation axis is reversed so that the traces appear in the same orientation as on the sky. Note that computations are not performed at elongations less than 12°.

(A color version of this figure is available in the online journal.)

efficiency have equal and opposite second derivatives at the TS, leading to the Thomson plateau; in the case of excess polarized radiance detection they have equal second derivatives at the TS, leading to a sharper maximum in intensity than would be observed via an s-scattering process with no angular dependence.

The difference in spatial kernel between *pB* and *B* enables location of individual solar wind features in three dimensions, and we have developed a theory of small feature location including the importance of S/N and kinematic effects in determining the precision to which location may be measured. The curvature of the TS breaks the front/back asymmetry that hinders attempts to accomplish the same thing in coronagraph images near the Sun. Features far from the TS are more readily located in three dimensions than are features near the TS, because the *pB*/*B* ratio varies more with the sky angle ξ far from the TS. An instrument that could measure the two relevant polarizations with comparable S/N to that of the *STEREO*/SECCHI imagers could locate the exit angle of small features within well under $10°$, greatly enhancing interpretation of the remote solar wind signal and potentially improving space weather prediction through direct location of Earth-directed features that are hard to measure geometrically (e.g., Lugaz 2010).

The *pB* signal is a differential signal that, by construction, eliminates unpolarized bright features from the field of view. This effect has been used historically in coronagraphs to remove stray light and sky light from the Thomson-scattering signal. Direct application in the heliosphere is more complex because the zodiacal light is polarized far from the Sun and hence is not removed by the *pB* calculation in the wide-field heliospheric imaging case. However, the zodiacal light is extremely stable both in degree of polarization and in overall intensity, leading to the possibility of direct absolute measurements of the Thomson-scattering signal using long baselines and *in situ* measurement of the average wind density; the additional stability of the polarization ratio further reduces the residual background variation below what may be achieved with a single measurement. Other diffuse light sources from near-Earth include orbital ram airglow and high altitude aurora, both of which we anticipate to be unpolarized and hence invisible in *pB*.

We have performed simple forward modeling of geometric structures similar to known solar wind structures to develop intuition about how a polarized heliospheric imager, if developed, will respond to those features. We find that one may expect significant, unambiguous *pB* signatures of the 3D location of large features, although analysis of such features is more complex than compact features whose geometry may be neglected. Techniques for, and the limits of, large-scale feature location in 3D from *pB* measurements require more detailed treatment and will be covered in the third paper of this series.

REFERENCES

Billings, D. E. 1966, A Guide to the Solar Corona (San Diego, CA: Academic)
Brown, T. M., Kimble, R. A., Ferguson, H. C., et al. 2000, AJ, 120, 1153
Brueckner, G. E., Howard, R. A., Koomen, M. J., et al. 1995, SoPh, 162, 357
Crifo, F., Picat, J. P., & Cailloux, M. 1983, SoPh, 83, 143
Davis, C. J., Davies, J. A., Lockwood, M., et al. 2009, GeoRL, 36, L08102
DeForest, C. E. 1995, PhD thesis, Stanford Univ.
DeForest, C. E., Howard, T. A., & McComas, D. M. 2012, ApJ, 745, 36
DeForest, C. E., Howard, T. A., & Tappin, S. J. 2011, ApJ, 738, 103
DeMastus, H. L., Wagner, W. J., & Robinson, R. D. 1973, SoPh, 100, 449
de Koning, C. A., & Pizzo, V. J. 2011, SpWea, 9, S03001
Dere, K. P., Wang, D., & Howard, R. 2005, ApJL, 620, L119
Dumont, R., & Sanchez, F. 1976, A&A, 51, 393
Eyles, C. J., Harrison, R. A., Davis, C. J., et al. 2009, SoPh, 254, 387
Eyles, C. J., Simnett, G. M., Cooke, M. P., et al. 2003, SoPh, 217, 319
Fisher, R. R., Lee, R. H., MacQueen, R. M., & Poland, A. I. 1981, ApOpt, 20, 1094
Gosling, J. T., Hildner, E., MacQueen, R. M., et al. 1975, SoPh, 40, 439
Harrison, R. A., Davis, C. J., Eyles, C. J., et al. 2008, SoPh, 247, 171
Hick, P., Jackson, B. V., & Schwenn, R. 1991, A&A, 244, 242
Hildner, E., Gosling, J. T., MacQueen, R. M., et al. 1975, SoPh, 42, 163
Howard, T. A., & DeForest, C. E. 2012, ApJ, 752, 130 (Paper I of this series)
Howard, T. A., DeForest, C. E., Tappin, S. J., & Odstrcil, D. 2013, ApJ, 765, 45 (Paper III of this series)
Howard, T. A., & Tappin, S. J. 2009, SSRv, 147, 31
Howard, T. A., & Tappin, S. J. 2010, SpWea, 8, S07004
Howard, T. A., Webb, D. F., Tappin, S. J., Mizuno, D. R., & Johnston, J. C. 2006, JGR, 111, A04105
Jackson, B. V. 1986, AdSpR, 6, 307
Jackson, B. V., Buffington, A., Hick, P. P., Bisi, M. M., & Clover, J. M. 2010, SoPh, 265, 257
Jackson, B. V., & Froehling, H. R. 1995, A&A, 299, 885
Jackson, B. V., & Webb, D. F. 1995, Proc. Sol. Wind, 8, 97
Jackson, J. D. 1962, Classical Electrodynamics (New York: Wiley)
Koomen, M. J., Detwiler, C. R., Brueckner, G. E., Cooper, H. W., & Tousey, R. 1975, ApOpt, 14, 743
Leinert, C., Bowyer, S., Haikala, L. K., et al. 1998, A&AS, 127, 1
Leinert, C., Link, H., Pitz, E., Salm, N., & Knueppelberg, D. 1975, RF, 19, 264
Leinert, C., & Pitz, E. 1989, A&A, 210, 399
Leinert, C., Richter, I., Pitz, E., & Planck, E. 1981, A&A, 103, 177
Leroy, J. L., Muler, R., & Poulain, P. 1972, A&A, 17, 301
Liu, Y., Davies, J. A., Luhmann, J. G., et al. 2010, ApJL, 710, L82
Lugaz, N. 2010, SoPh, 267, 411
Lugaz, N., Farrugia, C. J., Davies, J. A., et al. 2012, ApJ, 759, 68
Lugaz, N., Hernandez-Charpak, J. N., Roussev, I. I., et al. 2010, ApJ, 715, 499
Lyot, B. 1933, JRASC, 226, 265
Lyot, M. B. 1939, MNRAS, 99, 578
MacQueen, R. M. 1993, SoPh, 145, 169
MacQueen, R. M., Eddy, J. A., Gosling, J. T., et al. 1974, ApJL, 87, L85
Minnaert, M. 1930, ZA, 1, 209
Mizuno, D. R., Buffington, A., Cooke, M. P., et al. 2005, JGR, 110, A07230
Moran, T. G., & Davila, J. M. 2004, Sci, 305, 66
Moran, T. G., Davila, J. M., & Thompson, W. T. 2010, ApJ, 712, 453
Möstl, C., Farrugia, C. J., Kilpua, E. K. J., et al. 2012, ApJ, 758, 10
Poland, A. I., & Munro, R. H. 1976, ApJ, 209, 927
Richter, I., Leinert, C., & Planck, B. 1982a, A&A, 110, 111
Richter, I., Leinert, C., & Planck, B. 1982b, A&A, 110, 115
Rust, D. M. 1979, in Proc. Coll. Oslo, Physics of Solar Prominences (Oslo: Universitetet i Oslo), 252
Schuster, A. 1879, MNRAS, 40, 35
Tappin, S. J., Buffington, A., Cooke, M. P., et al. 2004, GeoRL, 31, L02802
Tappin, S. J., & Howard, T. A. 2009, SSRv, 147, 55
van de Hulst, H. C. 1950, BAN, 11, 135
van Houten, C. J. 1950, BAN, 11, 160
Vourlidas, A., & Howard, R. A. 2006, ApJ, 642, 1216
Wagner, W. J. 1982, AdSpR, 2, 203
Webb, D. F., Cheng, C.-C., Dulk, G. A., et al. 1980, in Solar Flares: A Monograph from Skylab Solar Workshop II, ed. P. Sturrock (Boulder, CO: Colorado Associated Univ. Press), 471
Webb, D. F., Howard, R. A., & Jackson, B. V. 1995, Proc. Sol. Wind VIII, 97
Webb, D. F., & Jackson, B. V. 1987, Proc. Sol. Wind VI, 2, 267
Webb, D. F., Mizuno, D. R., Buffington, A., et al. 2006, JGR, 111, A12101